Spatial Interpolation and Conditional Map Generation Using Deep Image Prior for Environmental Applications

Herbert Rakotonirina, Ignacio Guridi, Paul Honeine, Olivier Atteia, Antonin van Exem

Spatial Interpolation and Conditional Map Generation using Deep Image Prior for Environmental Applications*

Herbert Rakotonirina[1,2], Ignacio Guridi[3,4], Paul Honeine[1], Olivier Atteia[3], Antonin Van Exem[2]

[1] Univ Rouen Normandie, INSA Rouen Normandie, Université Le Havre Normandie, Normandie Univ, LITIS UR 4108, F-76000 Rouen, France
[2] Tellux, 72 rue Aristide Briand, 76650, Petit-Couronne, France
[3] EPOC (UMR 5805), CNRS, Univ. Bordeaux and Bordeaux INP, France
[4] SARPI Remediation, Meyzieu, France

Abstract

Kriging is the most widely used spatial interpolation method in geostatistics. For many environmental applications, kriging may have to satisfy the stationarity and isotropy hypothesis, and new techniques using machine learning suffer from a lack of labeled data. In this paper, we propose to use Deep Image Prior, which is a U-net-like deep neural network designed for image reconstruction, to perform spatial interpolation and conditional map generation without any prior learning. This approach allows to overcome the assumptions for kriging, as well as the lack of labeled data, while proposing uncertainty and probability above a certain threshold. The proposed method is based on a convolutional neural network that generates a map from random values by minimizing the difference between the output map and the observed values. From this new method of spatial interpolation, we generate n maps to have a map of uncertainty and a map of probability of exceeding the threshold. The conducted experiments demonstrate the relevance of the proposed methods for spatial interpolation, on both the well-known digital elevation model data and the more challenging case of pollution mapping. The obtained results with the three datasets demonstrate the competitive performance compared with state-of-the-art methods.

Keywords: geostatistics deep learning environmental data kriging soil pollution Geostatistical conditional simulation

*Rakotonirina, H., Guridi, I., Honeine, P. et al. Spatial Interpolation and Conditional Map Generation Using Deep Image Prior for Environmental Applications. Math Geosci 56, 949–974 (2024). https://doi.org/10.1007/s11004-023-10125-2

1 Introduction

Spatial interpolation is an inverse problem that consists in estimating new values from the spatial description of observed values. Geostatistics was founded in 1960 by the mathematician and geologist Matheron (1963). He formalized mathematically the work of Danie G. Krige who, in the 1950's, demonstrated that the variability of ore grade can be explained statistically (Krige, 1951).

Ordinary Kriging is the most widely used method in spatial interpolation for environmental data (Li et al., 2022b; Cui et al., 2016; Shad et al., 2009). However, kriging is a linear unbiased estimator often associated with Gaussian processes. This technique provides optimal results under assumptions of stationarity and isotropy. Those assumptions do not hold for environmental data, since they often have a sparse distribution, such as in groundwater contaminant plumes (Rivest et al., 2012). Even though some solutions have been proposed, such as log-normal transformation which transforms a skewed distribution into a normal distribution as demonstrated by the authors in Cressie (2006) and non-parametric models (Gribov and Krivoruchko, 2012), these methods do not generalize well in practice. Moreover, in environmental science, the problem is to estimate new values from the available observations that are spatially (Lu et al., 2015; Choi et al., 2022) or spatio-temporally distributed (Ahmed et al., 2018; van Zoest et al., 2020). These observation data are often relatively small as underlined by Carlon et al. (2001). Furthermore, the environmental data often have a right-skewed distribution due to the over-representation of values close to zero, namely pollution is often concentrated spatially.

Spatial interpolation methods can be roughly divided into three categories: non-geostatistical, geostatistical and hybrid approaches (Li and Heap, 2014). In the non-geostatistical methods for spatial interpolation, recent advances investigate generative networks (Goodfellow et al., 2020), allowing to ignore the stationarity assumption and to be scalable for large-scale dataset (Zhu et al., 2020; Gao et al., 2020). The deep learning approach also allows for the incorporation of auxiliary information to improve spatial interpolation, as demonstrated by Kirkwood et al. (2022). The image-driven approach is widely used in deep learning for spatial interpolation, as evidenced by studies such as (Suto et al., 2021; Yang et al., 2022). However, these methods require an important quantity of data. Another solution proposed by Sekulić et al. (2020) relies on a random forest to perform spatial interpolation, where the notion of spatial correlation is added using additional covariates defined by the n-nearest locations. The geostatistical methods consist in improving the processes of kriging. One of the most recent methods uses a dense neural network to adjust the variogram, allowing it to outperform the other variogram models (Li et al., 2022a). But although this method allows to automate the variographic analysis, this operation is time-consuming; Moreover, this method fails from freeing itself from the constraints related to the kriging. Hybrid approaches involve combining geostatistical and non-geostatistical methods, as demonstrated by Kartal and Sekertekin (2022). However, these approaches do not generalize well and their performances highly depend on the existing data.

For conditional map generation, the two main methods used in environmental science are Sequential Gaussian simulation (SGS) and sequential indicator simulation, as demonstrated in studies such as (Zhu et al., 2021; Huang et al., 2016). There also exist multivariate approaches, as shown by Emery and Silva (2009) and Madenova and Madani (2021). However, these approaches require significant computing capacities and require a Gaussian anamorphosis for the SGS when the data do not have a normal distribution.

In this paper, we propose to use an inpainting approach, which is well-suited for Deep Learning, to perform spatial interpolation. Both spatial interpolation and image inpainting are inverse problems that involve estimating new values based on observed values. Studies, such as (Keaomanee et al., 2020; Sapkal et al., 2016), have used kriging for image inpainting. The new spatial interpolation method that we propose uses a U-net-like convolutional neural network (CNN) inspired from recent advances in machine learning for inpainting, Deep Image Prior (DIP), proposed by Ulyanov et al. (2018), where the U-net architecture allows to reconstruct images from the remaining pixels without any backward learning. This is particularly important in our application domain because we do not have access to labeled training data. The proposed method is distribution-free, can bypass the assumption of stationarity, can handle a large-scale dataset, and is able to make interpolation from very limited numbers of samples. Moreover, using this U-net CNN as a main building block, we also propose a new method of conditional map generation, in the same spirit of conditional geostatistical simulations (Journel, 1974). To this end, we exploit the fact that the map output by the U-net architecture varies according to the randomly initialized convolution weights, as well as the random input. We therefore demonstrate how to generate the maximum, minimum and average maps, the map of the probability of exceeding a given threshold, as well as the pseudo-uncertainty map. These maps can be of great interest in environmental science.

In order to demonstrate the relevance of the proposed method for spatial interpolation, as well as the proposed conditional map generation, we provide comprehensive experiments by comparing our work with state-of-the-art methods on 3 datasets: The first one is a real data of digital elevation model (DEM) used in (Li et al., 2022a), the second one is from a hyperspectral analysis of hydrocarbon polluted soil cores, and the last one is a synthetic dataset generated from statistics and spatial descriptions of a real case of soil pollution with hydrocarbons. Our method has competitive results compared to the state-of-the-art techniques, including the ordinary kriging, log-normal ordinary kriging and the method with a variogram adjusted by a dense neural network.

The main contributions of this paper can be summarized as follows:

- We propose to perform a spatial interpolation by revisiting the DIP architecture proposed by Ulyanov et al. (2018) for image inpainting. To this end, we consider a U-net convolutional architecture that reconstructs the distribution of the variable of interest from the observed values. As we use deep learning, this allows us to free ourselves from the kriging constraints

related to the stationarity assumption and quantity of data. Moreover, deep learning also offers the possibility of doing calculations on GPU.

- Of great interest in environmental applications, we present a new method that generates multiple maps conditioned by the observations database. It allows to generate the maximum map, the minimum map, the average map, the map of the probability of exceeding a given threshold, and the pseudo-uncertainty map. The purpose of this approach is similar to conditional geostatistical simulations, which consists in doing a sequential simulation based on the probability density function and the variogram model of the variable of interest to have several maps as shown by Journel (1974).

- The proposed methods for spatial interpolation and conditional map generation do not rely on any assumption on the distribution of the data, making it of great interest for environmental applications. This is not the case of other methods that rely on some assumptions, such as kriging and sequential Gaussian simulation where a transformation of non-Gaussian data is necessary to have optimal results, under the assumption that the transformed data becomes Gaussian.

- This paper introduces two datasets for soil pollution analysis. The first dataset is from a hyperspectral analysis of hydrocarbon polluted soil cores. The second one is a synthetic dataset generated from statistics and spatial descriptions of a real case of soil pollution with hydrocarbons.

The rest of the paper is organized as follows. Next section presents the main contributions of this paper, which are divided into two subsections. Subsection 2.1 presents the new spatial interpolation method with the DIP U-net convolutional network as well as the details of this neural network architecture, and then, we develop in Subsection 2.2 the process steps of the new method of conditional map generation. In Section 3, we present the datasets in Subsection 3.1 before we provide extensive experimental results in Subsection 3.3, we show how we chose the hyperparameters in Subsection 3.2. Finally, Section 4 concludes this paper.

2 The proposed framework

The proposed framework is illustrated in Figure 1, divided into two main blocks: the proposed method for spatial interpolation and the conditional map generator. The proposed method for spatial interpolation is motivated by recent advances in image reconstruction techniques based on deep learning. The idea is to transform the spatial interpolation problem into an image reconstruction problem and to consider each point on the map as a pixel. The method, as proposed by Ulyanov et al. (2018), consists in generating a map $\hat{X}$ of the distribution of the variable of interest with a generative U-net neural network f from a random input z with similar dimension $\mathbb{R}^{H \times W}$ with W as width and H as

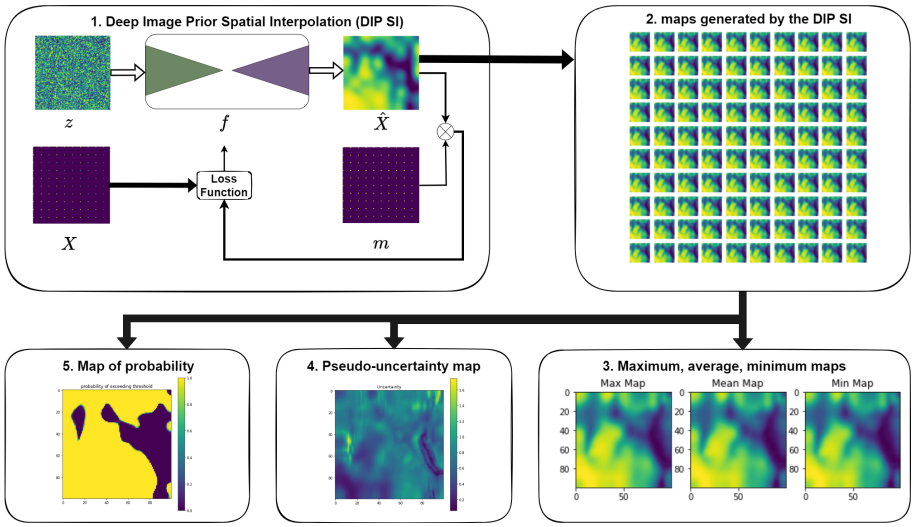

Figure 1: Illustration of the two methods proposed in this paper: the Deep Image Prior Spatial Interpolation (step 1) and the conditional map generation (step 2 to step 5). The U-net DIP SI architecture has a random input map z and $\hat{X}$ as output map with the same spatial resolution $\mathbb{R}^{W\times H}$ with W as width and H as height. The U-net function f is learned according to the mask $m \in \{0,1\}^{W\times H}$ and the samples value map $X \in \mathbb{R}^{W\times H}$. The DIP SI can generate several maps, as seen in step 2, and from these maps we can derive, as described in step 3, the maximum map, minimum map, average map, the map of the probability of exceeding a given threshold, and the map of the pseudo-uncertainty (steps 3, 4 and 5).

height, such that $\hat{X} = f(z)$. During the learning process, the generated map $\hat{X}$ is adjusted according to the observed values map X with a loss function. The result of the map generation depends on the random input and the convolution weights ω, which is randomly initialized. We propose in this paper to generate multiple maps which allows us to have a map of the mean, minimum, and maximum of the interpolated values. The n maps generated in this way give us a pseudo-uncertainty map by computing the standard deviation of each point in the n maps and the probability of exceeding the threshold by taking the number of times the point has exceeded the threshold among the n maps.

In the following, we describe in detail these two methods, namely the DIP U-net spatial interpolation method and the geostatistical conditional simulation based on it.

2.1 Spatial interpolation method

As shown in Figure 1, the foundation of the two proposed methods is the function f in the DIP Spatial Interpolation step. The architecture we used is similar

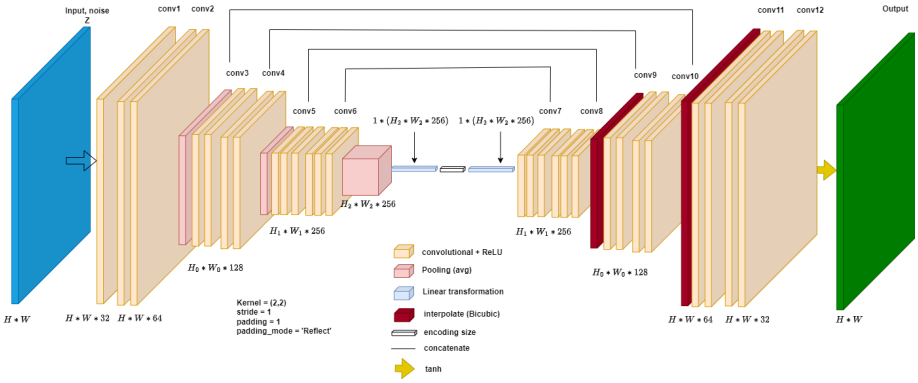

Figure 2: Convolutional U-net-like architecture for 2D spatial interpolation

to a U-net architecture.

The U-net is a CNN architecture essentially used for biomedical image segmentation (Ronneberger et al., 2015; El Jurdi et al., 2020). It is considered as an evolution of fully convolutional networks (Long et al., 2015), because it allows to work with less training images and provides more precise segmentation with a reduced computational complexity. The concept of using CNN layers to capture the spatial configuration of the map has been recently corroborated by Jo and Pyrcz (2022) to automatically adjust the variogram, showing that the kernel that moves through the whole map in each convolution layer can learn the spatial variability from the samples. While a classical U-net has as input an image and as output the segmentation of this image, we propose a different formalism in our case, namely for spatial interpolation: We have a random input z and the estimated map $\hat{X}$ as output.

As illustrated in Figure 2, the hourglass architecture of the proposed U-net can be divided into two parts: The contracting path (i.e., encoder part), which consists in reducing the dimension of the input z until obtaining the so-called latent vector, and the expansive path (i.e., decoder part), which consists in making the inverse operations to get the output map $\hat{X}$. Consequently, the hourglass architecture is similar to an autoencoder; However, our conducted operations aim to provide a generative neural network, which is not the case of autoencoders that learn to regenerate the input at the output.

2.1.1 The contracting path or encoder

The contracting path consists in a reduction of the dimension of the random input z, while increasing the feature information, to encode all the information in the output latent vector. To do this, we use a CNN composed of convolution and pooling layers. Convolution layers, each followed by a rectified linear unit (ReLU), act as a filter with a kernel that moves through the entire map. The transfer of information through the kernel between each convolution layer is

well suited to learn the spatial configuration, as corroborated recently by Jo and Pyrcz (2022). Pooling consists in shrinking the size of the map. There are two kinds of pooling: max pooling and average pooling.

2.1.2 The expansive path or decoder

In opposition to the contracting path, the expansive path or decoder increases the spatial dimension while decreasing the feature information. The expansive path is also composed of convolution layers but, instead of pooling operations, we have upsampling layers; Moreover, skip connections allow to concatenate them with high-resolution features from the concatenating path. Due to the nonlinearity introduced by the activation functions between the convolution layers, some information may be lost or distorted as the network progresses. The residual connection therefore makes it possible to preserve this complex information between different spatial scales, as recently corroborated by Tran and Yang (2022), resulting in a more accurate interpolated map with finer details.

Unlike image reconstruction tasks where the upsampling function with the best results is often the nearest function, this is not the case in our situation. Indeed, we have chosen to use the bicubic function[1], as opposed to bilinear or nearest interpolation, for many reasons. While the nearest upsampling method uses only the near values without any calculation and the bilinear method uses a linear polynomial to estimate the missing values, the bicubic method uses either Lagrange polynomials, cubic splines, or cubic convolution algorithm to perform a smoother surface interpolation. Thus, the bicubic interpolation gives smooth results like the ordinary kriging. This visual proximity of the results of this interpolation method with kriging is illustrated in Figure 3. Such proximity with the kriging results is of great interest because we have an extremely limited number of observed data in the case of most environmental applications. We will provide in Section 3 a comparative analysis and experimental results between the different interpolation functions.

The first step of the expansive path is to make a linear transformation of the encoded representation in order to have the first convolution layer, and then we proceed to the reverse operations of the contracting path by doing upsampling, with concatenations using skip connections, until we obtain the output dimension $\mathbb{R}^{H \times W}$. After the last convolution layer, we use the hyperbolic tangent as an activation function to get the output map of the distribution of interest values.

2.1.3 Loss function

The loss function is especially important in machine learning, as it is used to evaluate the ability of the model to learn from the training data. Our case is a bit specific compared to the classical case, because we have as output (of our U-net architecture) a 2D map with all the values, while we have only the

[1]More details on interpolation for downsampling and upsampling with PyTorch are available here: https://pytorch.org/docs/stable/generated/torch.nn.functional.interpolate.html

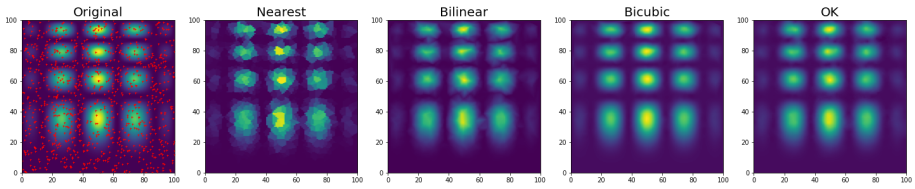

Figure 3: Illustration of results from the different interpolation methods (nearest, bilinear, bicubic) compared to the results of an ordinary kriging (OK). The sampled points are represented by the red crosses in the original image.

values of the samples to compare. To overcome this issue, we proceed to a Hadamard product $\otimes$ with the mask m to have the same elements in output of our algorithm and the sampled values, with $m \in \{0,1\}^{W \times H}$. The purpose of the loss function is to measure the difference between $\hat{X}$ and X, minimizing this difference enables to estimate the optimal parameters of the neural network f. The mean squared error as loss function $\mathcal{L}$ is defined as

$$\mathcal{L}(X, \hat{X}) = \left\| (X - \hat{X}) \otimes m \right\|^2. \tag{1}$$

2.2 Generative DIP U-net as alternative to geostatistical conditional simulation

The method described in Subsection 2.1 allows, like kriging, to perform a spatial interpolation from observed data. But for most environmental applications, spatial interpolation is not enough, and it is in this perspective that we propose to use the DIP U-net-like architecture as a conditional map generator.

The conditional geostatistical simulation was introduced by Journel (1974). This approach addresses the problem of non-integration of spatial correlations in simulation techniques. This simulation is conditional because the simulated values at the data locations are equal to the experimental values. And it is geostatistical as it considers the spatial correlation function, namely the variogram, in the simulation process. Sequential Gaussian simulation (SGS) and sequential indicator simulation are widely used methods for obtaining the spatial distribution of a variable in environmental science.

As for the geostatistical conditional simulation, our method can also generate multiple maps based on the observed values. Therefore, it is a generative CNN. Generative Adversarial Networks (GANs) are the most widely used generative networks in deep learning. The principle of GANs is to have two antagonistic networks, one to generate the data and one to differentiate the generated data from the real data; The goal is to generate data close to the real data by minimizing the distance between the distribution of the observed data and the generated data. Unfortunately, GANs require a very large amount of data to get good results, which is not the case in environmental applications where data is often limited and real training data may not be available. For example, in the

context of soil pollution, existing maps are already the result of processing, and we took the decision not to train our model on pre-interpolated data. Unlike GANs, the method we propose has only one generator network directly adjusted by the map of observed values X, allowing us to do the interpolation with a limited amount of data.

The steps of the proposed conditional map generation method are as follows:

1. The first step is to perform a spatial interpolation as described in Subsection 2.1

2. The second step consists in repeating the generation (step 1) n times to obtain n maps. Even if having the random input z to the f U-net function can add variability in the generation of the maps, this poses a problem of convergence of the algorithm. Indeed, the change of the input z at each generation can alter the performance of the CNN. To avoid this issue, we propose to seed z for each generation from the same input. This means that only the convolution weights ω are randomly initiated and vary according to the generations.

3. The n maps generated allow us to have 3 maps of the value of interest: the maximum map $\hat{X}_{max}$, where we take the maximum for each map of n generations, the minimum map $\hat{X}_{min}$ and the average map $\hat{X}_{avg}$ following the same principle, namely

$$\hat{X}_{max}(i,j) = \max\left\{\hat{X}_1(i,j),\ldots,\hat{X}_n(i,j)\right\} \quad (2)$$

$$\hat{X}_{min}(i,j) = \min\left\{\hat{X}_1(i,j),\ldots,\hat{X}_n(i,j)\right\} \quad (3)$$

$$\hat{X}_{avg}(i,j) = \frac{1}{n}\sum_{k=1}^{n}\hat{X}_k(i,j) \quad (4)$$

   where $\hat{X}_k$ represents each of the n generated maps, and i and j denote the coordinates of the points that constitute the maps. For the conditional geostatistical simulation, the mean map corresponds to the kriging interpolation map. Therefore, in the following we will use the mean map to compare with the kriging results.

4. The main advantage of kriging is to provide a prediction with the associated uncertainty. For environmental uses, the uncertainty map allows users to measure the reliability of the prediction and to help in the choice of the next areas to be sampled. In this paper, we propose a pseudo-uncertainty in the same spirit as in kriging. To this end, we consider the standard deviation between each value of the n maps to have the uncertainty map u, namely

$$u(i,j) = \sqrt{\frac{1}{n}\sum_{k=1}^{n}\left(\hat{X}_k(i,j) - \hat{X}_{avg}(i,j)\right)^2}. \quad (5)$$

With this formulation, we consider that the variation of $\hat{X}$ values mainly concerns the unsampled areas. However, this is not the case when the data do not have a normal distribution. Indeed, since we use the standard deviation, the highest values are over-represented in the uncertainty map.

5. In environmental applications, especially for pollution cartography, the threshold exceeding probability map is especially important. For example, for soil pollution, this map can help choose the area to be remediated. We propose to take the number of times the prediction $\hat{X}(i,j)$ exceeds the authorized threshold among the n maps generation, which gives

$$p(i,j) = P\left[\hat{X}_k(i,j) > \text{thresh}\right] \qquad \text{for all } k \in [1,n], \tag{6}$$

where p is the probability map and P represents the probability that a point exceeds the threshold.

3 Experiments and results

In this section, we first present the datasets and the fine-tuning of the hyperparameters, and then compare the proposed methods to other spatial interpolation methods, including ordinary kriging[2] (OK) (Cressie, 1988; Mälicke et al., 2021), a new kriging method that uses a dense neural network to automatically adjust the variogram (DNN-OK) (Li et al., 2022a) and log-normal ordinary kriging (LOK) (Journel, 1980; Yamamoto and Furuie, 2010; Balaban and Dengiz, 2018) for non-Gaussian data. We made a conditional geostatistical simulation with 1000 maps in order to compare the results with the proposed map generation method. Thus, this simulation gives us the map of averages, the map of uncertainty and the map of the probability of exceeding the threshold (denoted respectively Simu mean, Simu Proba, Simu Uncertainty).

3.1 Dataset and sampling method

We use three datasets to compare the results obtained by our method, as well as to fine-tune the hyperparameters of the U-net-like f function.

The first dataset is a real dataset of digital elevation model (DEM). This dataset was used by Li et al. (2022a). This dataset is composed of 4 areas, as shown in Figure 4 and in Table 1. Since the distributions of most of the datasets are much close to a normal distribution and they are not skewed, these datasets are suitable for the ordinary kriging, which is optimal for normal distributions. We also used this dataset as a test dataset for the analysis of the hyperparameters.

To show the efficiency of our method on the mapping of a hydrocarbon pollution, we use a dataset from the hyperspectral imagery conducted by Tellux. Indeed, Tellux proposes Machine Learning algorithms that match the index

[2]Ordinary kriging is done with SciKit GStat (https://scikit-gstat.readthedocs.io/)

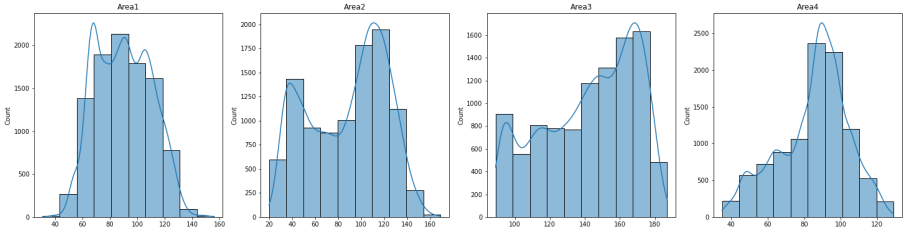

Figure 4: Distribution of the 4 DEM data areas

from the hyperspectral imagery, as shown by Achard and Elin (2019) and Kühn et al. (2004), with the hydrocarbon concentration from chemical analysis in laboratory. This dataset represents the diffusion of pollution in the soil at the scale of the borehole. Each pixel of the borehole image corresponds to $4mm$ by $4mm$. This dataset has a skewed distribution like the hydrocarbon pollution data, which is due to the over-representation of values near zero in the map. This provides images of hydrocarbon concentrations that constitute the second dataset.

The third dataset is a synthetic dataset created by replicating the main pollution variable (Total Petroleum Hydrocarbons in $mg.kg^{-1}$) from a real hydrocarbon polluted site with the Python library GSTools (Müller et al., 2022). The main pollution variable in $mg.kg^{-1}$ was created by a conditional simulation over the original dataset in a $100m \times 100m$ grid. First step is to transform the original variable from the real data into a log normal distribution. Then, the experimental variogram is created by calculating the average squared difference between each point separated at distance. The synthetic dataset was made from a simulation with the covariance model from Oliver and Webster (2015) and based on the experimental variogram of the log-transformed original variable (Sill). The covariance model with a semivariance γ of the spatial field is expressed as

$$\gamma(r) = \sigma^2 \left(1 - corr\left(s\frac{r}{l}\right)\right) + n, \tag{7}$$

where σ^2 is the variance, s is the scaling factor (if normalization), r is the range, l is the main correlation length and n is the nugget. The correlation function $corr(\cdot)$ depends on $s\frac{r}{l}$. Ordinary kriging is not optimal for this dataset, unlike the DEM dataset. Instead, we use LOK, which consists in doing a log-normal transformation of the variable of interest and then an inverse transformation after estimating with a corrective factor defined as

$$Z(x_0) = k_0 \exp(Y(x_0)) + \frac{\sigma_y^2}{2}, \tag{8}$$

where σ_y^2 is the kriging variance and k_0 is the correction factor given by the ratio between the sample mean and the back transformed mean (Journel, 1980; Yamamoto and Furuie, 2010; Balaban and Dengiz, 2018).

The prediction quality of kriging or other spatial interpolation methods depends strongly on the distribution of samples. For example, Mälicke et al. (2021) and Zhang et al. (2021) conducted a review of sampling strategies for kriging to improve its performance. Knowing this, we propose to use 4 different sampling strategies $\{S1, S2, S3, S4\}$ for each dataset, as illustrated in Figure 5. The sampling strategies $S1$ and $S2$ are composed of 100 points regularly distributed on the grid with a grid space of 10, the minimum value of the coordinates of the points for $S1$ is equal to (0,0), while for $S2$ the minimum value is $(3, 7)$. The sampling strategies $S3$ and $S4$ are also composed of 100 points but placed randomly on the map. Table 4 represents the p-value of the Kolmogorov-Smirnov test from the values for 4 sampling strategies for each dataset. The distribution is considered normal if the p-value is greater than 0.05.

For metrics to compare the results, we use the mean absolute error (MAE), defined as

$$MAE = \frac{1}{N} \sum_{i=1}^{N} \left| \hat{X}_i - X_i \right|, \tag{9}$$

and the root mean square error (RMSE), defined as

$$RMSE = \sqrt{\frac{1}{N} \sum_{i=1}^{N} \left(\hat{X}_i - X_i \right)^2}. \tag{10}$$

Since the second and third datasets have skewed distributions, we also use the mean absolute percentage error (MAPE), defined as

$$MAPE = \frac{100\%}{N} \sum_{i=1}^{N} \left| \frac{X_i - \hat{X}_i}{X_i} \right|. \tag{11}$$

In these expressions, N is the number of elements in the map, X is the ground truth map, and $\hat{X}$ the predicted map. It has the advantage of considering scale variation of the values to be estimated in the computation of the error, and thus gives the percentage of error compared to actual data. Therefore, this metric is widely used for environmental data. It can also be used as an evaluation index of fitting error for models, as shown by Zeng et al. (2016).

3.2 Hyperparameters

As our architecture is similar to an autoencoder architecture, the size of the vector at the bottleneck, namely the end of the encoder process, is also an hyperparameter. The most optimal size considers the learning time and the efficiency of the model. We evaluated 3 sizes of encoding $S \in \{10, 100, 1000\}$ and compared the MAE at the end of each map generation. The results show that $S = 10$ and $S = 1000$ have an average MAE quite close (see Figure 6), while knowing that the more the dimension of encoding is big the more the training time is important as highlighted in Table 5. For the following, we use the

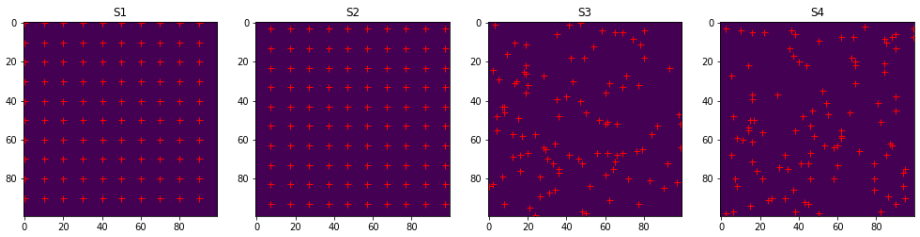

Figure 5: The 4 sampling strategies: $S1$ with $\{x_{\min} = 0; x_{\max} = 100; y_{\min} = 0; y_{\max} = 100; gridspace = 10\}$, $S2$ with $\{x_{\min} = 3; x_{\max} = 100; y_{\min} = 7; y_{\max} = 100; gridspace = 10\}$ and $S3$ and $S4$ are randomly generated.

encoding size $S = 10$, which is small for an encoding size but the skip connections between the encoder and decoder part allow to transfer the information between the layers without going through the encoding vector. However, we found that with synthetic data that have very skewed distributions even after log-normal transformation, as shown by the results of the Kolmogorov-Smirnov test (Table 4), the training of the U-net spatial interpolation does not converge. This is due to over-compressing the input by the encoding/contracting path. To overcome this issue, a larger encoding size is used with $S = 1000$ for data having complex distributions, namely skewed distributions as for the synthetic dataset. It is worth noting that the optimal size of the bottleneck of an autoencoder or U-net architecture is still an open problem.

In the contracting path, we have the choice between two downsampling techniques: average pooling and max pooling. We have proceeded to the same tests as for the encoder size to compare the two techniques. The results in Figure 7 show that the MAE between the two techniques are close, except for AREA 1 where average pooling gives better results. Therefore, we use average pooling for the three datasets.

The interpolation method used in the expansive path can also have an influence on the efficiency of our method. For the image reconstruction application proposed by Ulyanov et al. (2018), they used the nearest interpolation. In our case, we propose to use the bicubic interpolation, which gives better results as regards interpolation, as shows Figure 8.

3.3 Results on DEM data

The DEM data have a Gaussian distribution, which corresponds to what kriging expects and makes these experiments advantageous for ordinary kriging. The results in terms of MAE and RMSE, as given in Table 6 and Table 7, show that our method has competitive results compared to the two kriging methods. However, the results also show the fact that our model does not outperform other methods when considering random sampling. This is since kernel re-weighting only acts locally. As shown in Figure 5, for the random sampling strategies $S3$ and $S4$, there are zones where the number of samples is less than for other zones.

Table 1: Statistics (mean, standard deviation, minimum, first quartile, median, third quartile and maximum) for each area and by sampling strategy. The unit of data is the meter

		mean	std	min	25%	50%	75%	max
		89.98	**20.06**	**31.00**	**73.00**	**90.00**	**106.00**	**156.00**
	S1	90.13	20.61	58.00	69.75	89.50	106.25	133.00
Area1	S2	92.06	19.91	51.00	78.00	92.00	105.25	133.00
	S3	89.57	17.76	54.00	74.00	91.00	105.00	124.00
	S4	90.74	20.62	46.00	76.00	87.00	104.25	156.00
		88.37	**33.89**	**20.00**	**57.00**	**96.00**	**116.00**	**169.00**
	S1	82.77	33.24	26.00	48.00	87.50	111.00	143.00
Area2	S2	91.44	33.90	22.00	63.75	98.50	119.00	148.00
	S3	84.56	34.01	26.00	48.00	93.50	112.00	143.00
	S4	88.90	34.65	27.00	56.25	97.50	118.25	153.00
		142.61	**26.47**	**89.00**	**121.00**	**148.00**	**166.00**	**187.00**
	S1	143.81	26.49	92.00	121.50	148.00	166.25	184.00
Area3	S2	141.95	26.75	92.00	118.00	148.50	165.00	182.00
	S3	145.47	25.05	92.00	128.00	151.00	166.25	184.00
	S4	141.43	26.24	90.00	119.50	144.00	166.00	182.00
		85.32	**18.97**	**35.00**	**74.00**	**88.00**	**98.00**	**129.00**
	S1	84.38	18.93	38.00	69.75	87.00	97.00	120.00
Area4	S2	85.52	19.15	36.00	73.50	88.00	98.00	120.00
	S3	82.41	20.02	36.00	68.75	84.50	96.00	119.00
	S4	85.08	22.01	38.00	67.50	88.50	103.25	120.00

Under stationarity assumption, the variographic analysis of kriging assumes the fact that for each zone of the map the data have the same distribution, which allows it to have a better prediction than our method with a random sampling strategy.

We also note that the proposed method is more faithful to the sampled data. Figure 9 shows we have better results when the samples are closer to the real data, as for example in Area 4 where, for all the sampling techniques, the data remain close and thus the proposed method outperforms the other methods. Our method is thus more adapted for environmental applications, within the framework of a pollution mapping for example, because in this case pre-studies of the zone to be mapped make it possible to identify the most polluted zones.

3.4 Hydrocarbon concentration from hyperspectral images

The data used in this section is the result of a hydrocarbon pollution analysis of a borehole with hyperspectral imaging and supervised learning. And as shown in Table 4 after a log-normal transformation, for the 4 sampling strategies, the observed data have a normal distribution. We will therefore compare the

Table 2: Statistics (mean, standard deviation, minimum, first quartile, median, third quartile and maximum) for data from the hyperspectral image analysis by sampling strategy. The unit of data is $mg.kg^{-1}$

	mean	std	min	25%	50%	75%	max
Data	**1458.84**	**1666.16**	**50.00**	**216.53**	**835.72**	**2014.94**	**7585.36**
S1	1577.41	1755.77	50.00	294.93	886.15	2367.42	7373.25
S2	1470.34	1652.01	50.00	232.23	856.41	1818.84	5935.64
S3	1408.93	1600.01	50.00	315.15	818.34	1581.66	6902.00
S4	1183.12	1584.44	50.00	201.29	537.13	1338.42	7253.90

Table 3: Statistics (mean, standard deviation, minimum, first quartile, median, third quartile and maximum)for synthetic data generated from real hydrocarbon pollution by sampling strategy. The unit of data is $mg.kg^{-1}$

	mean	std	min	25%	50%	75%	max
Data	**5592.16**	**13578.21**	**50.00**	**50.00**	**139.23**	**2393.74**	**89815.74**
S1	6369.60	14835.25	50.00	50.00	204.98	3154.07	75177.96
S2	5014.45	11388.47	50.00	50.00	184.55	2254.67	63415.58
S3	5683.34	14290.26	50.00	50.00	201.17	1972.31	81369.32
S4	3558.30	9714.95	50.00	50.00	177.77	736.40	61007.99

proposed method to LOK but also to mean map of geostatistical conditional simulation. Table 8 shows competitive results with MAE and RMSE, while the MAPE results show that the proposed method outperforms geostatistical methods. The resulting map of the proposed method is remarkably close to the LOK result as shown by Figure 10, even though the proposed method does not require any prior spatial correlation analysis.

3.5 Synthetic Dataset

In this part, we analyze the relevance of the proposed method with a synthetic dataset created from real data of an industrial polluted soil with hydrocarbons.

We compared the MAE, RMSE and MAPE of the proposed method with LOK and the average map of the geostatistical simulation. Table 9 shows competitive results with these two methods. However, as shown in the Table 3, the data are unequally distributed between 50 $mg.kg^{-1}$ and 89815.74 $mg.kg^{-1}$, which explains the fact that the results differ according to the metrics, the results of the MAPE diverge from the results of the MAE and the RMSE. Indeed, the MAE and RMSE represent the average of the error and therefore the errors on the extremely high values would have much more weight in the results of these two metrics. On the other hand, the MAPE considers the values to be estimated to give a percentage error. To illustrate the effect of the extremely high values on the results of the MAE and RMSE, we have calculated the errors by concentration level for the sampling strategy $S2$, where the proposed method

Table 4: The P-values of the Kolmogorov-Smirnov test for all datasets by sampling strategies. The distribution is considered not normal if the p-value is smaller than 0.05 (values in bold).

	S1	S2	S3	S4
Area1	0.267	0.853	0.350	0.482
Area2	0.070	0.130	**0.049**	**0.040**
Area3	0.116	0.058	**0.020**	0.289
Area4	0.304	0.407	0.501	0.121
Hyperspectral image	**0.001**	**0.001**	**0.000**	**0.000**
Log hyperspectral image	0.135	0.091	0.287	0.182
Synthetic data	**0.000**	**0.000**	**0.000**	**0.000**
Log synthetic data	**0.000**	**0.000**	**0.000**	**0.000**

Table 5: Execution time and trainable parameters depending on the encoding size

Encoding Size	10	100	1000
Trainable Params	6×10^6	24×10^6	201×10^6
100 maps time generation	4min 16s	6min 30s	23min 5s

has a MAE and RMSE higher than the LOK and Simu mean. The results show that the DIP U-net method gives satisfactory results whatever the metrics for the values classes lower than $10000 mg.kg^{-1}$.

As given in Section 2.2, we also propose the map of the probability of exceeding a threshold. In the state-of-the-art, this map is generated by a conditional simulation based on the results of the variogram analysis, also called geostatistical simulation. For our case, we use the generated n maps as described in Subsection 2.2 to have the probability of exceeding the threshold. We can see from Figure 11 that the sampling strategy has a strong influence on the results of the probability exceeding threshold map. Moreover, since we have a limited number of samples, we cannot capture all polluted areas. We also note from Figure 11 that the proposed method of the probability of exceeding a threshold is much more straightforward than the geostatistical method with probability remarkably close to 1. This is confirmed by the confusion matrices given in Figure 12 where, for the two methods with a minimum probability of exceeding 1000 $mg.kg^{-1}$ at 0.9, 0.75 and 0.5; The closer this minimum probability is to 1, the more accurate the result of the proposed method is to the actual data. In any case, both methods give an accuracy close to 95%, which is sufficient to perform a fairly accurate soil remediation.

For most environmental applications, the uncertainty map is particularly important, it allows to evaluate the estimated values but also to choose the coordinates of new locations to estimate in order to reduce the uncertainty. We have compared the method proposed by the uncertainty map from a geostatistical simulation with 1000 maps. Knowing that the interest of the uncertainty

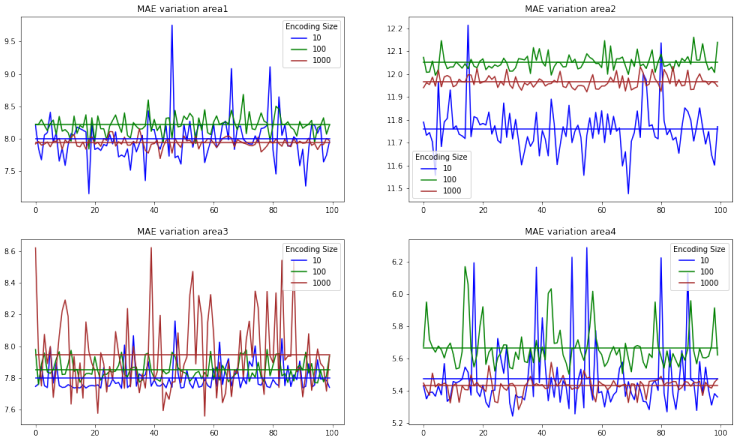

Figure 6: The MAE (vertical axis) variations over 100 maps (horizontal axis) of the results obtained by the proposed method according to the encoding size $S \in \{10, 100, 1000\}$ for the 4 DEM areas. The horizontal lines in each figure represent the mean of the MAE values for the 100 map

map is to show the locations where the estimation method is imprecise, we propose to compare the uncertainty map with the absolute error map of the estimation. Figure 13 shows that our method gives an uncertainty map consistent with the error map. The proposed method of uncertainty map has results quite close to the geostatistical simulation for the sampling strategies $S1$ and $S2$. However, we find that for random sampling strategies, and especially for $S3$, the geostatistical simulation gives results of the uncertainty more faithful to the absolute error map. For random sampling strategies, we also find with the proposed method that the largest variations correspond to observed data, which should not be the case.

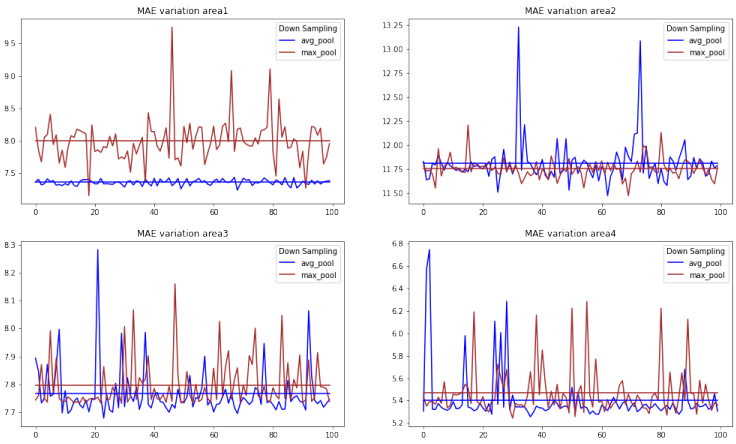

Figure 7: The MAE (vertical axis) variations over 100 maps (horizontal axis) of the results obtained by the proposed method according to the shrinking technique (average pooling and max pooling) for the 4 DEM areas. The horizontal lines in each figure represent the mean of the MAE values for the 100 map

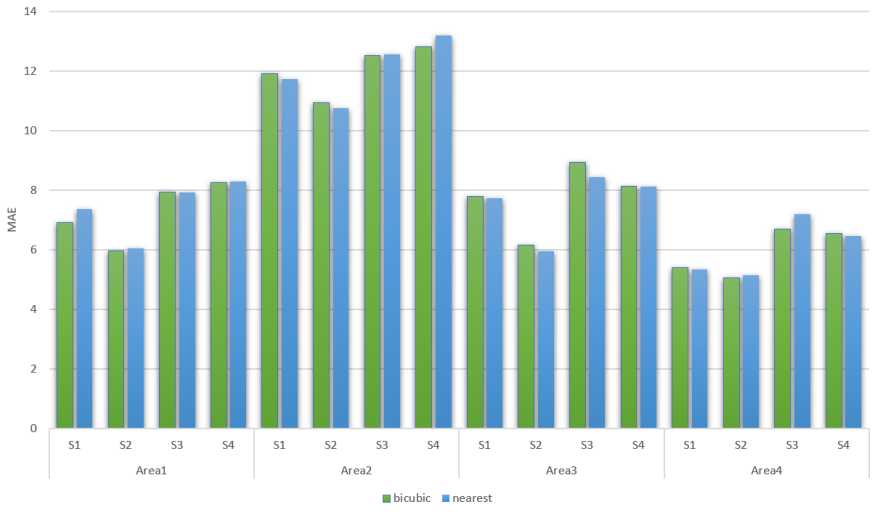

Figure 8: The MAE between bicubic and nearest interpolation results for the 4 DEM areas and the 4 sampling strategies

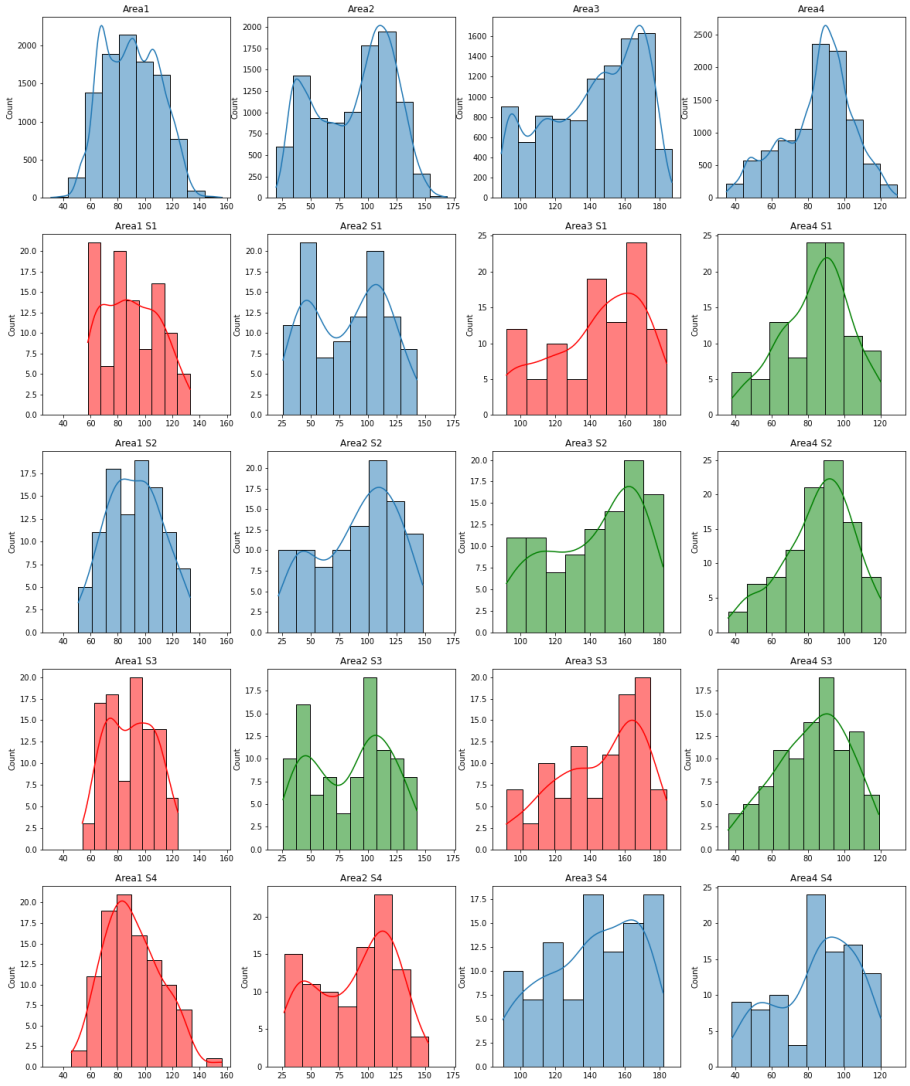

Figure 9: The distributions of the 4 areas and the distributions of the 4 different sampling strategies. The histogram is green when the proposed method is better than kriging by more than 5% and for the reds, it is kriging that is better by more than 5%.

Table 6: The MAE of the different methods depending on the sampling strategy

	Sampling	OK	DNN-OK	This paper
Area 1	S1	6.33	6.13	6.92
	S2	6.16	6.21	5.96
	S3	7.20	13.86	7.94
	S4	7.16	11.98	8.25
Area 2	S1	10.87	10.94	11.49
	S2	10.57	10.63	10.93
	S3	13.32	13.86	12.53
	S4	10.46	11.31	12.82
Area 3	S1	8.22	8.10	7.79
	S2	7.01	7.17	6.15
	S3	7.88	11.27	8.93
	S4	8.13	10.00	8.13
Area 4	S1	5.67	5.69	5.39
	S2	5.40	5.34	5.05
	S3	7.27	8.63	6.68
	S4	6.79	6.93	6.55

Table 7: The RMSE of the different methods depending on the sampling strategy

	Sampling	OK	DNN-OK	This paper
Area 1	S1	9.44	9.42	9.89
	S2	9.10	9.21	8.48
	S3	10.67	54.28	11.57
	S4	10.23	52.05	12.21
Area 2	S1	14.90	15.05	15.89
	S2	14.55	14.73	15.23
	S3	18.29	19.62	17.88
	S4	14.24	15.96	17.77
Area 3	S1	13.78	13.44	12.93
	S2	10.03	10.41	8.64
	S3	10.53	25.05	13.17
	S4	11.76	19.94	12.89
Area 4	S1	7.83	8.04	7.67
	S2	7.25	7.34	7.27
	S3	11.04	15.89	9.73
	S4	9.98	10.32	9.08

Table 8: The MAE, RMSE and MAPE of the hyperspectral image dataset, comparing the LOK with the proposed method.

	Sampling	LOK	Simu Mean	This paper
MAE	S1	179.10	329.12	183.23
	S2	200.54	310.12	186.75
	S3	266.12	282.93	288.07
	S4	256.24	277.85	253.45
RMSE	S1	275.21	532.75	277.26
	S2	348.03	520.20	336.37
	S3	519.44	570.30	596.15
	S4	437.04	458.64	432.74
MAPE	S1	54.61%	55.13%	38.97%
	S2	36.92%	38.70%	20.89%
	S3	67.16%	50.48%	42.59%
	S4	71.65%	52.63%	37.87%

Table 9: The MAE, RMSE and MAPE of the synthetic dataset, comparing the log-normal ordinary kriging, the mean map from geostatistical simulation, and the proposed spatial interpolation method (mean of generated map).

	Sampling	LOK	Simu mean	This paper
MAE	S1	2920.75	2805.06	2755.88
	S2	3074.50	3087.46	3129.42
	S3	3267.93	4392.19	4163.58
	S4	3263.31	3333.99	3297.94
RMSE	S1	8561.42	8238.80	8104.82
	S2	8744.60	8638.47	9192.44
	S3	9314.54	13021.07	11683.91
	S4	9854.03	9215.22	9734.36
MAPE	S1	79.84%	71.81%	37.74%
	S2	69.31%	72.18%	46.10%
	S3	63.55%	107.28%	77.31%
	S4	45.45%	72.06%	45.80%

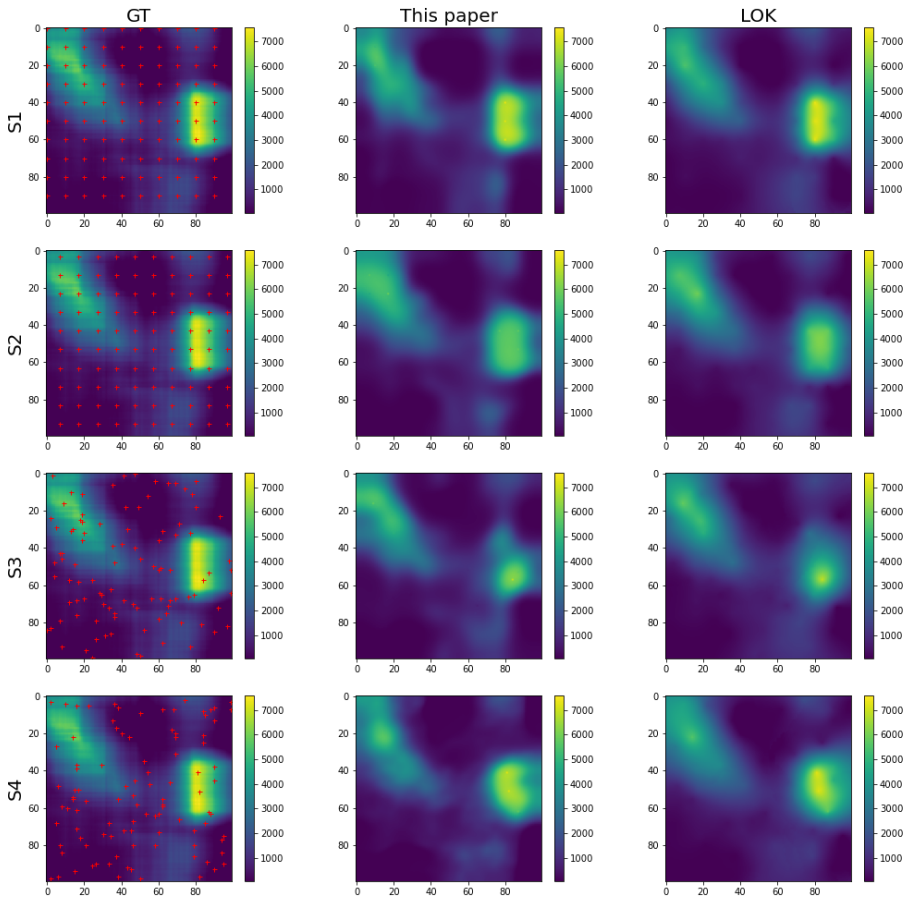

Figure 10: Maps of the results of the proposed method (This paper) compared to the results of the log-normal ordinary kriging (LOK) for hyperspectral hydrocarbon concentration image dataset represented in first column Ground Truth (GT). The red crosses represent the sampling points.

Table 10: The MAE, RMSE and MAPE by concentration level of the synthetic dataset with the $S2$ sampling strategy, comparing to lognormal ordinary kriging, the mean map from geostatistical simulation, and the proposed spatial interpolation method (mean of generated map).

	Concentration level ($mg.kg^{-1}$)	LOK	Simu mean	This paper
MAE	0-500	89.15	84.69	53.38
	500-1000	495.97	474.48	428.84
	1000-10000	4105.09	3950.44	3658.75
	+10000	14958.65	15048.49	15808.14
RMSE	0-500	243.82	233.57	175.45
	500-1000	900.10	867.49	760.80
	1000-10000	7304.44	7095.41	6556.00
	+10000	20422.65	20773.21	22112.91
MAPE	0-500	68.98%	66.13%	32.07%
	500-1000	70.18%	67.08%	60.50%
	1000-10000	106.18%	102.04%	93.23%
	+10000	53.55%	51.87%	52.21%

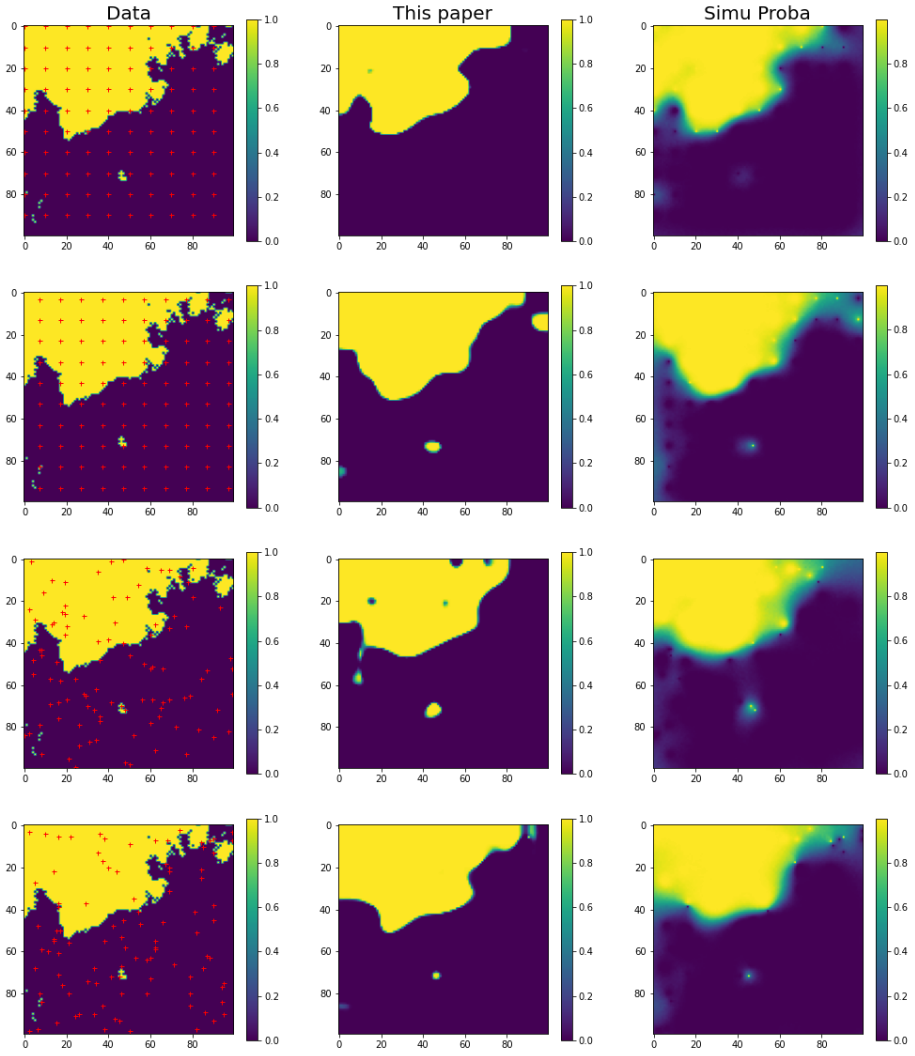

Figure 11: Illustration of the results of the probability map of exceeding 1000 $mg.kg^{-1}$ between the proposed method and the geostatistical conditional simulation for the synthetic data of hydrocarbon pollution. The first column represents the map classification of data according to whether it exceeds the threshold of 1000 $mg.kg^{-1}$ or not. The red crosses represent the observed data.

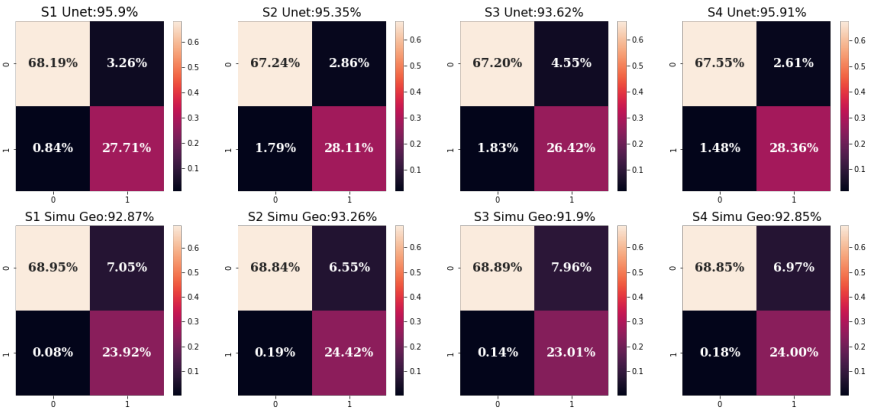

(a)

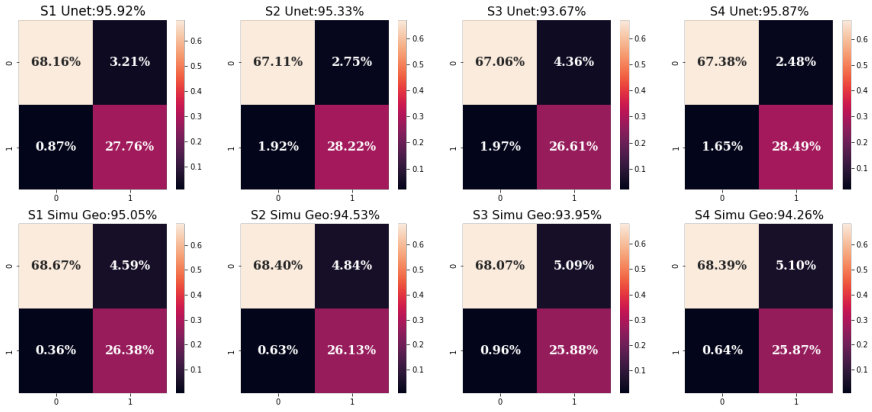

(b)

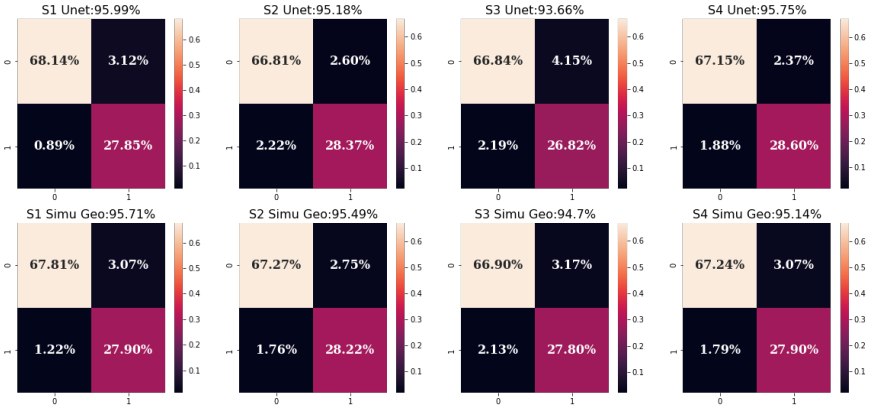

(c)

Figure 12: Illustration of the different confusion matrices between the actual classification of the data and the classification given by the probability of exceeding 1000 $mg.kg^{-1}$ greater than 0.9 (a), 0.75 (b) and 0.5 (c) for the proposed method (Unet) and the geostatistical simulation by sampling strategy. The value 0 indicates that the threshold is not exceeded and 1 represents the opposite (namely, detection).

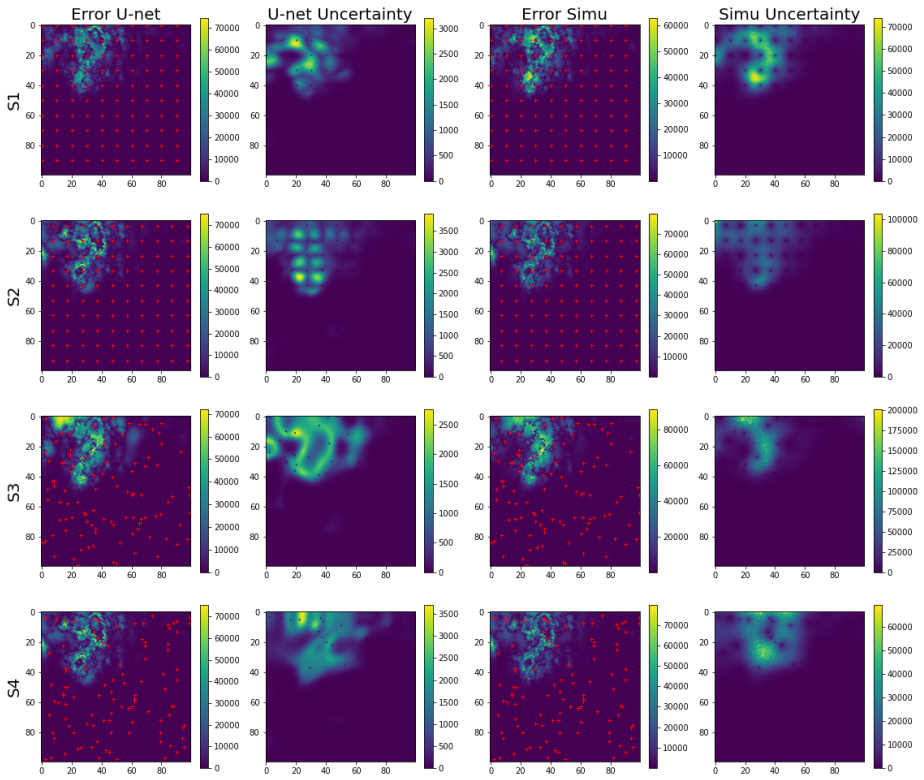

Figure 13: The first column is the absolute error map between the real map and the mean map of the proposed method (U-net), while the absolute error map of the average of the geostatistical simulation is on the third column. The uncertainty maps of the proposed method, compared to the results of a conditional geostatistical simulation, are given in the second and fourth columns. The red crosses represent the sampling points.

4 Conclusion

In this paper, we have proposed a method for spatial interpolation, as well as a new conditional generation method using Deep Image Prior U-net-like architecture. This approach was motivated by recent advances in image reconstruction methods. Moreover, the proposed method does not need any prior training to perform well. We have also seen that convolution networks can capture the spatial configuration of the data, which allows us to go directly to interpolation without worrying about spatial correlation, while for ordinary kriging, the interpolation results depend on the analysis of the spatial correlation. Regarding the experimental results, we evaluated our method on 3 datasets, and we saw that we have competitive results compared to ordinary kriging methods, whether it is the classic method or the method with a variogram adjusted by a dense neural network. Unlike kriging, our method works with any data distribution and requires less computation to perform so it is scalable for large-scale data, on top of that, to generate the 100 maps as we did in the experiments with DEM data, it took 4 minutes using Tesla P100-PCIE-16GB GPU from Google Co-Lab. We have also seen through the probability exceeding threshold maps that the proposed generation method gives a result quite close to the geostatistical simulation, even if the method gives a more straightforward probability map. We have seen that our method does not perform very well when it comes to random sampling because the kernel only captures local spatial patterns. The possibilities for improvement of our methods therefore consist in adding spatial correlation information to the neural networks. This can be done by using a loss function that includes the spatial notion, or by adapting the size of the kernel according to the correlation distance at the sampled points. It is also possible to take advantage of very recent advances in inpainting, a very dynamic field of research, to improve the performance of our model. Another way of improving our method is to propose, as co-kriging does, the possibility of having two variables of interest.

5 Acknowledgment

The authors would like to thank the agency of ecological transition ADEME in France and TELLUX company for the funding of this research work. We would like to express our sincere gratitude to the anonymous reviewers for their valuable feedback and constructive comments, which significantly contributed to the enhancement of the quality and clarity of this manuscript. We also want to thank Gregory CHATEL for proposing the idea of using deep learning image reconstruction to do spatial interpolation.

6 Conflict of interest

The authors declare that they have no conflict of interest.

References

Achard V, Elin C (2019) Automatic mapping of hydrocarbon pollution based on hyperspectral imaging. In IGARSS 2019-2019 IEEE International Geoscience and Remote Sensing Symposium, IEEE, 5768–5771

Ahmed S O, Mazloum R, Abou-Ali H (2018) Spatiotemporal interpolation of air pollutants in the greater cairo and the delta, egypt. Environmental research 160:27–34

Balaban M, Dengiz B (2018) Lognormal ordinary kriging metamodel in simulation optimization. Operations Research and Applications: An International Journal (ORAJ) 5(1):1–12

Carlon C, Critto A, Marcomini A, Nathanail P (2001) Risk based characterisation of contaminated industrial site using multivariate and geostatistical tools. Environmental pollution 111(3):417–427

Choi H, Kim H, Yeom S, Hong T, Jeong K, Lee J (2022) An indoor environmental quality distribution map based on spatial interpolation methods. Building and Environment 213:108880

Cressie N (1988) Spatial prediction and ordinary kriging. Mathematical geology 20(4):405–421

Cressie N (2006) Block kriging for lognormal spatial processes. Mathematical Geology 38(4):413–443

Cui Y Q, Yoneda M, Shimada Y, Matsui Y, et al. (2016) Cost-effective strategy for the investigation and remediation of polluted soil using geostatistics and a genetic algorithm approach. Journal of Environmental Protection 7(01):99

El Jurdi R, Petitjean C, Honeine P, Abdallah F (2020) BB-UNet: U-Net with bounding box prior. IEEE Journal of Selected Topics in Signal Processing 14(6):1189–1198, ISSN 1941-0484

Emery X, Silva D A (2009) Conditional co-simulation of continuous and categorical variables for geostatistical applications. Computers & Geosciences 35(6):1234–1246

Gao Y, Liu L, Zhang C, Wang X, Ma H (2020) SI-AGAN: Spatial interpolation with attentional generative adversarial networks for environment monitoring. Frontiers in Artificial Intelligence and Applications 325:8

Goodfellow I, Pouget-Abadie J, Mirza M, Xu B, Warde-Farley D, Ozair S, Courville A, Bengio Y (2020) Generative adversarial networks. Communications of the ACM 63(11):139–144

Gribov A, Krivoruchko K (2012) New flexible non-parametric data transformation for trans-gaussian kriging. In Geostatistics Oslo 2012, Springer, 51–65

Huang J h, Liu W c, Zeng G m, Li F, Huang X l, Gu Y l, Shi L x, Shi Y h, Wan J (2016) An exploration of spatial human health risk assessment of soil toxic metals under different land uses using sequential indicator simulation. Ecotoxicology and environmental safety 129:199–209

Jo H, Pyrcz M J (2022) Automatic semivariogram modeling by convolutional neural network. Mathematical Geosciences 54(1):177–205

Journel A (1980) The lognormal approach to predicting local distributions of selective mining unit grades. Journal of the International Association for Mathematical Geology 12(4):285–303

Journel A G (1974) Geostatistics for conditional simulation of ore bodies. Economic Geology 69(5):673–687

Kartal S, Sekertekin A (2022) Prediction of modis land surface temperature using new hybrid models based on spatial interpolation techniques and deep learning models. Environmental Science and Pollution Research 29(44):67115–67134

Keaomanee Y, Heednacram A, Youngkong P (2020) Implementation of four kriging models for depth inpainting. ICT Express 6(3):209–213

Kirkwood C, Economou T, Pugeault N, Odbert H (2022) Bayesian deep learning for spatial interpolation in the presence of auxiliary information. Mathematical Geosciences 54(3):507–531

Krige D G (1951) A statistical approach to some basic mine valuation problems on the witwatersrand. Journal of the Southern African Institute of Mining and Metallurgy 52(6):119–139

Kühn F, Oppermann K, Hörig B (2004) Hydrocarbon index–an algorithm for hyperspectral detection of hydrocarbons. International Journal of Remote Sensing 25(12):2467–2473

Li J, Heap A D (2014) Spatial interpolation methods applied in the environmental sciences: A review. Environmental Modelling & Software 53:173–189

Li Y, Baorong Z, Xiaohong X, Zijun L (2022a) Application of a semivariogram based on a deep neural network to ordinary kriging interpolation of elevation data. Plos one 17(4):e0266942

Li Z, Tao H, Zhao D, Li H (2022b) Three-dimensional empirical bayesian kriging for soil pahs interpolation considering the vertical soil lithology. Catena 212:106098

Long J, Shelhamer E, Darrell T (2015) Fully convolutional networks for semantic segmentation. In Proceedings of the IEEE conference on computer vision and pattern recognition, 3431–3440

Lu Q, Luo Q S, Li H, Liu Y D, Gu J D, Fei Lin K (2015) Characterization of chlorinated aliphatic hydrocarbons and environmental variables in a shallow groundwater in shanghai using kriging interpolation and multifactorial analysis. PloS one 10(11):e0142241

Madenova Y, Madani N (2021) Application of gaussian mixture model and geostatistical co-simulation for resource modeling of geometallurgical variables. Natural Resources Research 30:1199–1228

Mälicke M, Möller E, Schneider H D, Müller S (2021) mmaelicke/scikit-gstat: A scipy flavoured geostatistical variogram analysis toolbox

Matheron G (1963) Principles of geostatistics. Economic geology 58(8):1246–1266

Müller S, Schüler L, Zech A, Heße F (2022) Gstools v1. 3: a toolbox for geostatistical modelling in python. Geoscientific Model Development 15(7):3161–3182

Oliver M A, Webster R (2015) Basic steps in geostatistics: the variogram and kriging. Springer

Rivest M, Marcotte D, Pasquier P (2012) Sparse data integration for the interpolation of concentration measurements using kriging in natural coordinates. Journal of hydrology 416:72–82

Ronneberger O, Fischer P, Brox T (2015) U-net: Convolutional networks for biomedical image segmentation. In International Conference on Medical image computing and computer-assisted intervention, Springer, 234–241

Sapkal M S, Kadbe P K, Deokate B H (2016) Image inpainting by kriging interpolation technique for mask removal. In 2016 International Conference on Electrical, Electronics, and Optimization Techniques (ICEEOT), IEEE, 310–313

Sekulić A, Kilibarda M, Heuvelink G, Nikolić M, Bajat B (2020) Random forest spatial interpolation. Remote Sensing 12(10):1687

Shad R, Mesgari M S, Shad A, et al. (2009) Predicting air pollution using fuzzy genetic linear membership kriging in gis. Computers, environment and urban systems 33(6):472–481

Suto K, Bannai S, Sato K, Inage K, Adachi K, Fujii T (2021) Image-driven spatial interpolation with deep learning for radio map construction. IEEE Wireless Communications Letters 10(6):1222–1226

Tran Q N, Yang S H (2022) Video frame interpolation via down–up scale generative adversarial networks. Computer Vision and Image Understanding 220:103434

Ulyanov D, Vedaldi A, Lempitsky V (2018) Deep image prior. In Proceedings of the IEEE conference on computer vision and pattern recognition, 9446–9454

van Zoest V, Osei F B, Hoek G, Stein A (2020) Spatio-temporal regression kriging for modelling urban no2 concentrations. International journal of geographical information science 34(5):851–865

Yamamoto J K, Furuie R d A (2010) A survey into estimation of lognormal data. Geociências 29(1):5–19

Yang G, Chen Z, Ndzi D L, Yang L, Al-Hassani A H, Paul D C, Duan Z, Chen J (2022) Deep spatial interpolation of rain field for uk satellite networks. IEEE Transactions on Antennas and Propagation 71(2):1793–1803

Zeng W, Yang Y, Xie H, Tong L j (2016) Cf-kriging surrogate model based on the combination forecasting method. Proceedings of the Institution of Mechanical Engineers, Part C: Journal of Mechanical Engineering Science 230(18):3274–3284

Zhang X, Lu Z, Cheng K (2021) Ak-ds: An adaptive kriging-based directional sampling method for reliability analysis. Mechanical Systems and Signal Processing 156:107610

Zhu D, Cheng X, Zhang F, Yao X, Gao Y, Liu Y (2020) Spatial interpolation using conditional generative adversarial neural networks. International Journal of Geographical Information Science 34(4):735–758

Zhu L, Zhang L, Wang J, Lv J (2021) Combining finite mixture distribution, receptor model, and geostatistical simulation to evaluate heavy metals pollution in soils: Source and spatial pattern. Land Degradation & Development 32(6):2105–2115